Accuracy of Diffusing-Wave Spectroscopy Theories

Douglas J. Durian
University of Pennsylvania, djdurian@physics.upenn.edu

Accuracy of Diffusing-Wave Spectroscopy Theories

Abstract

Random walk computer simulations are reported for the electric field autocorrelation of photons transmitted through multiple-scattering slabs. The results are used as a benchmark for judging the accuracy of competing theories of diffusing-wave spectroscopy (DWS), and also for distinguishing between errors introduced from the approximation of diffusive photon transport and from the continuum approximation that the total square wave-vector transfer of a transmitted photon is proportional to its path length in the material. An important conclusion is that these errors partially cancel, giving accuracies on the order of a few percent for typical experimental situations. Detailed comparisons are made as a function of optical thickness, boundary reflectivity, as well as scattering anisotropy; guidelines are generated for optimizing the analysis of actual DWS data in terms of the dynamics of individual scattering sites.

Disciplines

Physical Sciences and Mathematics | Physics

Comments

At the time of publication, author Douglas J. Durian was affiliated with University of California, Los Angeles. Currently, he is a faculty member at the Physics Department at the University of Pennsylvania.

Accuracy of diffusing-wave spectroscopy theories

D. J. Durian

Department of Physics, University of California, Los Angeles, California 90024-1547

(Received 21 October 1994)

Random walk computer simulations are reported for the electric field autocorrelation of photons transmitted through multiple-scattering slabs. The results are used as a benchmark for judging the accuracy of competing theories of diffusing-wave spectroscopy (DWS), and also for distinguishing between errors introduced from the approximation of diffusive photon transport and from the continuum approximation that the total square wave-vector transfer of a transmitted photon is proportional to its path length in the material. An important conclusion is that these errors partially cancel, giving accuracies on the order of a few percent for typical experimental situations. Detailed comparisons are made as a function of optical thickness, boundary reflectivity, as well as scattering anisotropy; guidelines are generated for optimizing the analysis of actual DWS data in terms of the dynamics of individual scattering sites.

PACS number(s): 82.70.−y, 05.40.+j, 42.62.Fi

I. INTRODUCTION

Quasielastic light scattering techniques have proven extremely useful for characterizing the dynamics, and indirectly the structure, of nearly transparent materials such as dilute solutions of macromolecules or colloidal particles [1–4]. For useful information to be readily extracted, samples must be sufficiently thin, dilute, or well index matched that incident photons scatter at most once from the random dielectric inhomogeneities before exiting. Recently, the technique of diffusing-wave spectroscopy (DWS) has been developed [5–7] to extend the application of these traditional single-scattering techniques to materials such as concentrated colloidal suspensions [8–12], foams [13–15], and emulsions [16,17], which all multiply scatter the incident light. Even though typical experimental samples are optically thick in that they appear white and do not permit photons to pass through without scattering many times, the scattering is "weak" in the sense that successive events are uncorrelated and that the contribution from photons traversing separate paths add incoherently. While this tremendously simplifies the theories of DWS, they are still highly complex and involve several uncontrolled approximations and adjustable parameters. The purpose of this paper is to assess the accuracy of DWS predictions for the normalized electric field autocorrelation function $g_1(\tau) \equiv \langle E(0)E^*(\tau) \rangle / \langle |E|^2 \rangle$, by means of computer simulation and to generate guidelines for the analysis of transmission experiments. Results are obtained for the accuracy of both characteristic decay scale and functional form of $g_1(\tau)$ for a variety of experimental situations; typically, both are on the order of a few percent. The details of such results reported here should be especially important for the experimentalist wishing to know and to minimize the systematic error introduced during data analysis.

Standard DWS theories

The assumptions and approximations in the theories of DWS are first highlighted with a brief discussion of the statics and dynamics of multiple light scattering; points not explicitly referenced are covered in greater detail in published reviews [18–20]. Consider, then, the fate of a coherent beam of photons directed toward a slab of material containing particles that scatter light, and assume that absorption is negligible. The intensity of the unscattered portion of the incident beam will decay exponentially with distance into the medium according to the scattering mean free path l_s, whose value is set by both the number density and total scattering cross section of the suspended particles $l_s = 1/\rho\sigma$. In the multiple-scattering regime, the sample is very large in comparison with l_s so that photons scattered away from the incident beam typically experience many more scattering events before exiting. The transport mean free path l^*, which enters into diffusion theory treatment of this process, is related to the scattering mean free path according to how strongly photons are deflected from their unscattered, or forward, direction: $l^* = l_s / \langle 1 - \cos\theta \rangle$, where θ is the deflection angle and the average is taken over the scattering form factor for the probability of scattering by θ. Many materials of interest scatter light preferentially in the forward direction, and it is not unusual for l^* to be ten or more times greater than l_s. Physically, l^* represents the typical distance a photon travels before its propagation direction is completely randomized, and can hence be thought of as the typical step size in a random walk. For example, consider photons that are transmitted through a multiple-scattering slab of thickness L. The typical number of completely random steps of size l^* is $O(L/l^*)^2$, and each is composed on average of l^*/l_s separate scattering events.

In the photon-correlation version of dynamic light scattering experiments, both in the single- and multiple-scattering regimes, a portion of the scattered light comparable to a few speckled spots is observed with a photomultiplier tube. Relative motion of the scattering sites then causes significant intensity fluctuations that can be characterized by a temporal intensity autocorrelation function $\langle I(0)I(\tau) \rangle$, which is an average over the time labeled 0. The corresponding normalized electric field

autocorrelation function $g_1(\tau) \equiv \langle E(0)E^*(\tau)\rangle/\langle|E|^2\rangle$ is given by the Siegert relation $\langle I(0)I(\tau)\rangle/\langle I\rangle^2 = B + \beta|g_1(\tau)|^2$, where the base line B is identically 1 unless there are slow drifts in the laser intensity, and the intercept β is a number less than 1 that depends mainly on the number of speckles observed. For the case of single scattering from a large number of noninteracting uncorrelated particles, the field autocorrelation function may be computed:

$$\langle E(0)E^*(\tau)\rangle = \langle|E|^2\rangle e^{-q^2\langle\Delta r^2(\tau)\rangle/6} , \qquad (1)$$

where $\mathbf{q}=\mathbf{k}_{\text{out}}-\mathbf{k}_{\text{in}}$ is the change in wave vector, and $\langle\Delta r^2(\tau)\rangle$ is the mean square displacement of the particles. Since the scattering sites move slowly by comparison with the speed of light, the scattering is quasielastic in that the magnitudes of the incident and scattered wave vectors are essentially equal, $|\mathbf{k}_{\text{in}}|=|\mathbf{k}_{\text{out}}|\equiv k$. The magnitude of the change in wave vector is therefore set by the scattering angle $q=2k\sin(\theta/2)$. Note that the correlation function in Eq. (1) thus decays on a time scale set by how long it takes the particles to move on the order of $1/q$, which is comparable to the wavelength of light.

As recognized in Ref. [5], the electric field autocorrelation function can be similarly computed for an arbitrary path α of a photon that experiences n independent scattering events from n uncorrelated scattering sites in an optically dense medium:

$$\langle E_\alpha(0)E_\alpha^*(\tau)\rangle = \langle|E_\alpha|^2\rangle\exp\left[-\sum_{i=1}^{n}q_{\alpha,i}^2\langle\Delta r^2(\tau)\rangle/6\right] , \qquad (2)$$

where $q_{\alpha,i}$ is the change in wave vector for the ith scattering event in the path α. Besides the independence of the particle motions and of scattering events, this result assumes only that the electric fields can be treated as complex Gaussian random variables. If one further assumes that the fields due to different paths add incoherently, which is an excellent approximation in practice, then the total normalized electric field correlation function is found by the weighted average of Eq. (2) over all possible light paths:

$$g_{1Y}(x) = \int_0^\infty P(Y)e^{-xY/3}dY , \qquad (3)$$

where $x\equiv k^2\langle\Delta r^2(\tau)\rangle$ is the dimensionless mean square displacement of the particles, and $P(Y)$ is the probability density for any path α with any number n of scattering events to have dimensionless total square wave-vector transfer

$$Y\equiv\sum_{i=1}^{n}q_{i,a}^2/2k^2 = \sum_{i=1}^{n}(1-\cos\theta_{i,\alpha}) . \qquad (4)$$

The decay of the field correlation function with x as given by Eqs. (3) and (4) cannot be calculated analytically; it may, however, be evaluated numerically via computer simulation, as in Ref. [21] for the case of backscattering from progressively thicker slabs.

To make analytical progress, note from Eq. (4) that for paths consisting of a very large number n of scattering events, Y can be approximated by averaging over the scattering form factor

$$Y\cong n\langle 1-\cos\theta\rangle = \frac{nl_s}{l^*} = \frac{s}{l^*}\equiv S , \qquad (5)$$

where s is the total length of the light path. In this large-n continuum limit, Y is the independent of the scattering length l_s, and its value indicates the number of completely random steps in the path. If the experimental geometry is such that all paths contributing to Eq. (3) satisfy the large-n limit, then the normalized electric field autocorrelation function can be accurately approximated by

$$g_{1S}(x) = \int_0^\infty P(S)e^{-xS/3}dS , \qquad (6)$$

where $P(S)$ is the probability density for a detected light path to have dimensionless length $S\equiv s/l^*$. The great advantage of Eq. (6) over Eqs. (3) and (4) is that for a given experimental geometry $P(S)$, and hence $g_{1S}(x)$, can be evaluated analytically by using a diffusion approximation for photon transport. Equation (6) has therefore been the basis for computing correlation functions in the standard theory of DWS.

As an experimental probe of internal dynamics, the most important geometry for DWS is transmission through a multiple-scattering slab of material whose thickness L is both significantly smaller than its width and significantly greater than the transport mean free path l^* of light. The optical configuration is usually such that there is no discrimination against transmitted light paths on the basis of their lateral excursion, which is on average $O(L)$. Either the sample is illuminated with a plane wave and speckle is formed with light that emerges from a point on the opposite face [19,20], or, more simply and efficiently, the sample is illuminated with a beam much smaller than the sample width and speckle is formed with light that emerges from over the entire opposite face [22]. The standard DWS result based on Eq. (6) and diffusion theory is then

$$g_{1\text{DWS}}(x) = \frac{(L/l^*)+2z_e}{z_p+z_e}\frac{\sinh[z_p\sqrt{x}]+z_e\sqrt{x}\cosh[z_p\sqrt{x}]}{(1+z_e^2x)\sinh[(L/l^*)\sqrt{x}]+2z_e\sqrt{x}\cosh[(L/l^*)\sqrt{x}]} , \qquad (7)$$

where z_p and z_e are phenomenological parameters of order 1, respectively called the penetration depth and extrapolation length ratios. The boundary conditions assumed in Eq. (7) are that the density of diffusing photons extrapolates linearly to zero at a distance $z_e l^*$ outside both faces of the sample. Diffusion theory cannot, however, adequately describe the propagation of photons close to the sample boundaries because there the velocity distribution is not isotropic; the value of the extrapolation length ratio is chosen as $z_e=(\frac{2}{3})(1-R)/(1+R)$, where R is an average diffuse boundary

reflectivity, to best compensate for this shortcoming [23,24]. The source of diffusing photons assumed in Eq. (7) is located exactly at $z_p l^*$ in from the edge of the sample; in practice, the value of the penetration depth ratio is usually taken to be $z_p = 1$ on the grounds that l^* is the average distance required for the propagation direction of the incident photons to first become completely randomized. In reality, diffusing photons are created over a continuous range of penetration depths up to $O(l^*)$ by photons that scatter away from the incident beam and become completely randomized, either instantly as in the case $l^* = l_s$ of isotropic scattering, or gradually by successive scattering events as in the case $l^* > l_s$ of anisotropic scattering. It is therefore more appropriate that Eq. (7) be averaged over z_p according to the joint probability $\exp(-z_p)(z_p + z_e)/(L/l^* + 2z_e)$ for a diffusing photon to be created at $z_p l^*$ and then to be transmitted through the slab [22]

$$g_{1\langle DWS\rangle}(x) = \frac{[(L/l^*) + 2z_e]\sqrt{x}/(1-x)}{(1+z_e^2 x)\sinh[(L/l^*)\sqrt{x}] + 2z_e\sqrt{x}\cosh[(L/l^*)\sqrt{x}]} . \tag{8}$$

This averaging scheme is, in principle, correct only for the case of isotropic scattering. For anisotropic scattering, diffusion theory cannot describe the gradual conversion of incident photons to diffusing photons and so while no source term can be truly satisfactory, the exponential form assumed for Eq. (8) is properly broad and may reasonably be expected to be an improvement over the single-penetration depth approximation of Eq. (7). However, this need not be the case: for highly anisotropic scattering, no diffusing photons will be created near the incident boundary and so the source term will be peaked and may be better described by a point source.

The functional forms of Eqs. (7) and (8) both give reasonable results when compared with experiments on well-characterized samples [18,19]; however, their range of validity and accuracy are difficult to quantitatively assess because there are so many adjustable parameters. For example, in using Eq. (7) on colloidal suspensions with purely diffusive dynamics, $\langle \Delta r^2(\tau)\rangle = 6D\tau$ with D being the diffusion coefficient of the particles, there are at least eight parameters whose values can be adjusted to improve the agreement between theory and experiment: D, l^*, z_e, and z_p in Eq. (7); the baseline and intercept in the Siegert relation; and the choices for upper and lower limits of the fitting interval. Furthermore, choice of weighting and the order in which parameters are adjusted can also influence fitting results, as can the presence of a small amount of absorption or a finite coherence length

for the incident radiation. See Refs. [20,22] for recent comparisons of theory and experiment on known systems.

As for the trends expected on theoretical grounds, note that the diffusion theory approximations embodied by z_e and z_p, or its average, all become better in the limit that the sample is very thick in comparison with l^*, since the photon velocity distribution is then isotropic across all but an insignificant portion of the sample. Indeed for sufficiently large L/l^*, Eqs. (7) and (8) both reduce to the simple form $g_1(x) = \sqrt{(L/l^*)^2 x}/\sinh\sqrt{(L/l^*)^2 x}$ independent of the value of z_e or the treatment of z_p. For the usual experimental case of samples of intermediate optical thickness, $L/l^* \sim 10$, the treatment of source and boundary terms are important issues, unfortunately, and the ultimate accuracy of the diffusion theory results, as well as their failure for decreasing L/l^* independent of the continuum approximation, have not previously been determined. Even so, it is possible to circumvent the *a priori* inadequacies of the diffusion approximations by application of the radiative transfer theory of photon transport, which explicitly relaxes the assumption that the photon velocity distribution is everywhere isotropic [25]. The resulting correlation transfer equation can be solved formally, but must be evaluated numerically; for transmission through a slab with isotropic scattering and no boundary reflections, an accurate analytical approximations is given by

$$g_{1CT}(x) \cong \frac{[(L/l^*) + \sqrt{\frac{4}{3}}]\sqrt{x}\,[(1-x/3)/(1-x)]^2}{(1+x/3)\sinh[(L/l^*)\sqrt{x}] + 2\sqrt{x/3}\cosh[(L/l^*)\sqrt{x}]} . \tag{9}$$

Apart from the last algebraic factor in the numerator, this expression is identical to Eq. (8) if an extrapolation length ratio of $\sqrt{\frac{1}{3}}$ is used instead of the best diffusion theory value of $z_e = \frac{2}{3}$; the actual numerical prefactors appearing in Eq. (9) depend, however, on an arbitrary choice of parameters used to approximate an exponential integral in the theory (see Eqs. (46) and (47) of Ref. [25]). Note, also, that both Eqs. (8) and (9) become unphysical near a singularity at $x = 1$. Generalization of the correlation transfer approach to anisotropic scattering with nonzero boundary reflectivity has not yet been reported.

II. RANDOM WALK SIMULATIONS

The accuracy of the approximate diffusion theory and correlation transfer solutions of Eq. (6) for the case of transmission through a slab geometry, as well as the continuum approximation of Eq. (5) on which Eq. (6) is based, can be directly tested by computer simulation. Since in transmission the vector nature of photons and the interference of different paths can be neglected, as in the above theories, photon propagation can be modeled by random walks. The general procedure adopted here is

therefore, as in previous computer simulation tests of diffusion theory predictions for multiple light scattering processes [21,24], to collect statistics for a series of walkers, or photons, which are launched one at a time in the $+z$ direction and allowed to wander by a series of steps, or scattering events, until exiting the slab at either $z = 0$ or $z = L$. For typical experimental systems, the scattering is anisotropic and the reflectivity of the boundary is nonzero; it is important, therefore, to explicitly include these effects. When a simulated scattering event happens to land outside the sample, there is thus assumed to be an angle-independent probability R for the photon to specularly reflect from the boundary such that the current step length is unchanged; for optically thin slabs, this includes the possibility of multiple reflections from opposite faces. The rules for generating random steps are such that the scattering can be either isotropic or peaked in the forward direction. For the case of isotropic scattering in three dimensions, the change in z coordinates is simply $\Delta z = \Delta s \mu_z$ where step size and direction are, respectively,

$$\Delta s = -l^* \ln N_{\text{rand}}, \quad \mu_z \equiv \cos\theta_z = 2N_{\text{rand}} - 1 , \quad (10)$$

both N_{rand} are random numbers generated uniformly between zero and 1, but by different algorithms, and θ_z is the angle between the propagation and $+z$ directions. For each such step, the total dimensionless square wave-vector transfer is increased by

$$\Delta y \equiv 1 - \cos\theta = 1 - \mu_z \mu_{z0} - \sqrt{(1 - \mu_z^2)(1 - \mu_{z0}^2)} \sin\varphi_z , \quad (11)$$

where μ_{z0} is the $+z$ direction cosine of the previous step, and $\varphi_z = 2\pi N_{\text{rand}}$ is an azimuthal angle around the $+z$ direction. For the more general case of anisotropic scattering, the random steps are generated more directly using the Henyey-Greenstein scattering form factor [26]:

$$\Delta s = -l_s \ln N_{\text{rand}} ,$$

$$\mu = \frac{1}{2\langle\mu\rangle}\left[(1 + \langle\mu\rangle^2) - \left[\frac{1 - \langle\mu\rangle^2}{1 - \langle\mu\rangle + 2\langle\mu\rangle N_{\text{rand}}}\right]^2\right] ,$$

$$\varphi = 2\pi N_{\text{rand}} , \quad (12)$$

where $\mu \equiv \cos\theta$ is the cosine of the scattering angle, whose average is input as $\langle\mu\rangle = 1 - (l_s/l^*)$ according to the desired degree of anisotropy, and φ is an azimuthal angle about the unscattered direction. The Henyey-Greenstein form factor is often used to model the characteristics of actual scattering media, and represents an approximation of the true scattering form factor by a Legendre polynomial expansion that sums up to $F(\mu) = \frac{1}{2}(1 - \langle\mu\rangle^2)(1 + \langle\mu\rangle^2 - 2\langle\mu\rangle\mu)^{-3/2}$. It is easily verified that $\int_{-1}^{1} F(\mu) d\mu = 1$, $\int_{-1}^{1} F(\mu)\mu \, d\mu = \langle\mu\rangle$, and that the rule in Eq. (12) reproduces $F(\mu)$ if N_{rand} is uniformly drawn between zero and 1. For all simulations, lengths are measured in terms of the scattering length so that the prefactor of the logarithms in Eqs. (10) and (12) is -1, thus saving one multiplication per scattering event.

A. Path length vs total square wave-vector transfer

The simplest quantities to collect statistics on are the path lengths and the total square wave-vector transfers. According to the continuum approximation of Eq. (5), the dimensionless path length $S \equiv \sum_{i=1}^{n} \Delta s_i / l^*$ should be equal to the dimensionless total square wave-vector transfer $Y \equiv \sum_{i=1}^{n} (1 - \cos\theta_i)$ for paths consisting of a sufficiently large number n of scattering events. To directly test this assertion, and in particular to demonstrate the nature of it failure for small n, Fig. 1 shows scatter plots of S/Y vs S for 1000 transmitted walks and 4 combinations of boundary reflectivity and scattering anisotropy at a fixed optical thickness of $L/l^* = 10$. In all cases, the average values of S and Y are on the order of $(L/l^*)^2 = 100$, and the ratio S/Y clusters around an average value noticeably greater than 1. While the continuum approximation is therefore not strictly valid, there is a certain statistical agreement between S and Y that improves for longer S and for increasing degrees of scattering anisotropy and boundary reflectivity, all of which give rise to a larger number of scattering events. The discrepancy between S and Y is most pronounced for shorter paths, as expected, because they consist of a smaller number of scattering events. Note for example that the shortest paths occur for photons that snake their way across the slab by scattering only a few times close to the forward direction; while the path length can never be less than the slab thickness, the value of Y can be arbitrarily small and the ratio S/Y can be arbitrarily large. Such snakelike photon paths must be made statistically insignificant, through increased slab thickness, level of anisotropy, or boundary reflectivity, for the continuum approximation to be valid.
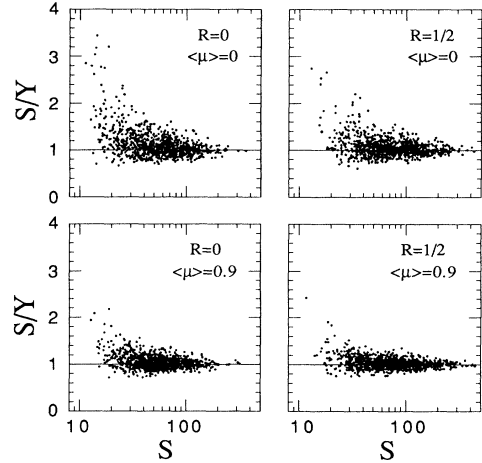

FIG. 1. Scatter plots comparing path length $(S \times l^*)$ with total square wave-vector transfer $(Y \times 2k^2)$ for 1000 random walks transmitted through slabs of fixed optical thickness $L/l^* = 10$; results are labeled according to the boundary reflectivity R, and the average cosine of the scattering angle $\langle\mu\rangle$. In the limit of a large number of scattering events per path, S and Y should be equal; this continuum approximation holds on average except for short, snakelike, paths.

In order to gauge the prevalence of snakelike photon paths and their effect on the continuum approximation, the average path length can be compared with the average total square wave-vector transfer. The fractional difference of $\langle S \rangle$ from $\langle Y \rangle$ as a function of increasing optical thickness is thus shown in Fig. 2 for two values of boundary reflectivity and several degrees of scattering anisotropy: $\langle \mu \rangle = 0$ using Eqs. (9) and (10), and $\langle \mu \rangle = 10^{-6}$, $\frac{2}{3}$, $\frac{9}{10}$, and $\frac{29}{30}$ using Eq. (12). The agreement between the isotropic and nearly isotropic results serves as a check on the simulation algorithms and codes. The data in Fig. 2 are based on as many as 4 000 000 transmission events, or as few as 6250, depending on the optical thickness and the scattering anisotropy. The magnitude of the difference of $\langle S \rangle$ and $\langle Y \rangle$ simulation data is seen never to exceed 10%, even for slabs as thin as $L/l^* = 3$, and to vanish rapidly with increasing optical thickness. A constant improvement factor of roughly 2 is obtained by increasing the boundary reflectivity from zero to $\frac{1}{2}$. Also, a modest amount of scattering anisotropy significantly improves the agreement of $\langle S \rangle$ and $\langle Y \rangle$; however, the benefit of increasing anisotropy saturates at a factor of roughly 2 for anisotropies greater than about $l^*/l_s \approx 10$. The simulations in the next section will therefore focus on the two cases of $l^*/l_s = 1$ and $l^*/l_s = 10$. Note in Fig. 2 that for at least 1% agreement between $\langle S \rangle$ and $\langle Y \rangle$, the minimum optical thickness is never more than $L/l^* \cong 14$, in the case of isotropic scattering and no boundary reflections, but can be as small as $L/l^* \cong 7$, as in the typical experimental situation of $R \approx \frac{1}{2}$ and $l^*/l_s \approx 10$, and could be smaller for even higher boundary reflectivities. Significant error due to

the continuum approximation will therefore be present in the analysis of actual data on slabs thinner than these optical thicknesses.

B. Temporal autocorrelations

Even if $\langle S \rangle$ and $\langle Y \rangle$ happen to agree to 1% for a given system, the normalized electric field autocorrelation functions computed from Eqs. (3) and (6) can differ by substantially more. Since for transmission through a slab, the distribution functions are peaked and $\langle Y \rangle$ and $\langle S \rangle$ are well defined, the short-time small-x limiting form of the correlation functions can be found by expansion of the exponential factors in Eqs. (3) and (6), giving $g_{1Y}(x) = 1 - x \langle Y \rangle /3 + \cdots$ and $g_{1S}(x) = 1 - x \langle S \rangle /3 + \cdots$, respectively. At sufficiently short times, where all paths contribute equally according to a simple average, $g_{1S}(x)$ will therefore have the same initial functional form as $g_{1Y}(x)$, but will decay faster since $\langle S \rangle$ always exceeds $\langle Y \rangle$. At longer times, by contrast, the exponential factors cannot be expanded and will weight the smaller-S and smaller-Y paths more heavily. This will cause the functional forms of $g_{1Y}(x)$ and $g_{1S}(x)$ to differ because, as seen in the scatter plots of Fig. 1, paths with small values of S tend to have even smaller values of Y. In short, $g_{1Y}(x)$ should begin its decay more slowly than would be predicted by the small-n approximation of $g_{1S}(x)$ according to the difference between $\langle S \rangle$ and $\langle Y \rangle$, while at longer times $g_{1Y}(x)$ should decay progressively more slowly than $g_{1S}(x)$ because of the presence of snakelike photon paths. This is confirmed by the simulation results shown in Fig. 3 for $g_{1Y}(x)$ and $g_{1S}(x)$, computed by simulation directly from Eqs. (3) and (6), at fixed $L/l^* = 10$ and four combinations of scattering anisotropy and boundary reflectivity. The plots consist of three to five runs each having 10^6 transmission events; since the separate runs are indistinguishable, the plotted curve widths are an upper limit on error due to insufficient sampling of the S and Y distributions. As expected, the correlation functions are roughly exponential in x with decay constants set by $\langle S \rangle \gtrsim \langle Y \rangle \approx (L/l^*)^2$, and $g_{1Y}(x)$ has a more slowly decaying functional form than $g_{1S}(x)$. As further expected from Fig. 1, agreement between $g_{1Y}(x)$ and $g_{1S}(x)$ improves with increasing boundary reflectivity and scattering anisotropy. Note that $1\frac{1}{2}$ decades of decay of the field autocorrelation, as shown in Fig. 3, corresponds to three decades in the intensity autocorrelation and is the limit of ordinary experiments. Even though $\langle S \rangle$ and $\langle Y \rangle$ differ by no more than 2% for the cases shown, the correlation functions can differ by up to factor of 2 over the experimentally measurable range, and would differ by even more could the measurement range be extended.

Apart from the above comparison of $g_{1Y}(x)$ with $g_{1S}(x)$ as a test of the large-n continuum approximation, it is important also to judge the accuracy of the analytic predictions of Eqs. (7)–(9) since they are used in analysis of experimental data and are all based on further approximations. Toward this end, Fig. 4 shows the difference $\Delta g_1(x)$ of the correlation function predictions from simu-
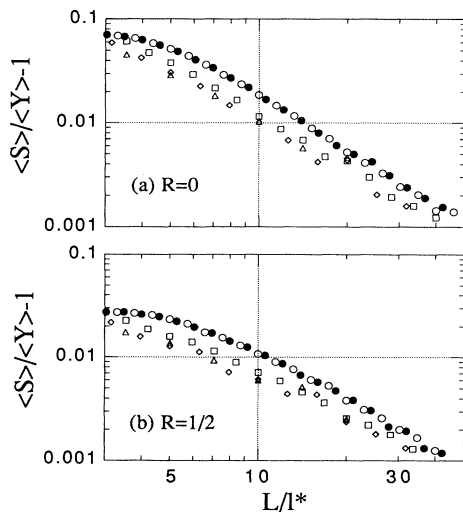
FIG. 2. Fractional difference of the average dimensionless path length $\langle S \rangle$ from the average dimensionless total square wave-vector transfer $\langle Y \rangle$ for random walks transmitted through slabs of optical thickness L/l^*. Open circles, solid circles, squares, diamonds, and triangles are for walks where the average cosine of the scattering angle is $\langle \mu \rangle = 0$, 10^{-6}, $\frac{2}{3}$, $\frac{9}{10}$, and $\frac{29}{30}$, respectively; this corresponds to $l^*/l_s = 1$, $1/(1-10^{-6})$, 3, 10, and 30.
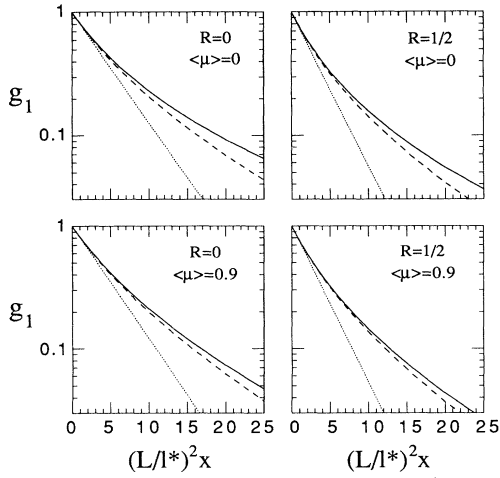
FIG. 3. The normalized electric field autocorrelation function $g_1(x)$ as a function of the dimensionless dynamical variable $x = k^2 \langle \Delta r^2(\tau) \rangle$ for transmission through four slabs of optical thickness $L/l^* = 10$. Solid curves are for the benchmark $g_{1Y}(x)$, computed by simulation directly from Eqs. (3) and (4), and the dashed curves are for the continuum approximation $g_{1S}(x)$ computed by simulation directly from Eq. (6); the dotted lines represent the small-x behavior $\ln[g_{1Y}(x)] \approx -\Gamma_1 x$. Note that the decays are nearly exponential in x with a decay constant set by $(L/l^*)^2$, the typical number of completely random steps in an average transmission event. Also, $g_{1Y}(x)$ has more upward curvature than $g_{1S}(x)$ since, as seen in Fig. 1, there are more small-Y paths than small-S paths. Plots are labeled according to the boundary reflectivity R and the average cosine of the scattering angle $\langle \mu \rangle$.
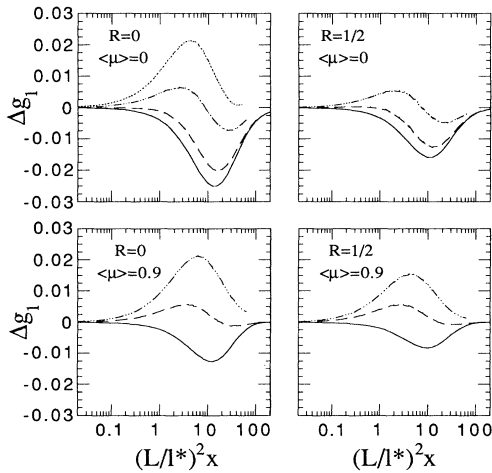

FIG. 4. Difference between the approximate and benchmark correlation functions $\Delta g_1 = g_1 - g_{1Y}$ as a function of the dimensionless dynamical variable $x = k^2 \langle \Delta r^2(\tau) \rangle$ for transmission through four slabs of optical thickness $L/l^* = 10$. The solid curves are for $g_{1S}(x)$ of Eq. (6); the dashed curves are for $g_{1\mathrm{DWS}}(x)$ of Eq. (7); the dash-dotted curves are for $g_{1\langle\mathrm{DWS}\rangle}(x)$ of Eq. (8); and the dotted curve is for $g_{1\mathrm{CT}}(x)$ of Eq. (9). Plots are labeled according to the boundary reflectivity R, and the average cosine of the scattering angle $\langle \mu \rangle$.

lation results of the benchmark $g_{1Y}(x)$ for the same four special cases of $L/l^* = 10$ considered previously in Figs. 1 and 3. Since the correlation functions all start at 1 and decay toward zero, the differences vanish for both large and small $(L/l^*)^2 x$, and in Fig. 4 reach a maximum of $\Delta g_1(\tau) \approx 0.02$ near $(L/l^*)^2 x \approx 10$, where $g_{1Y}(\tau) \approx 0.2$ is still easily measurable. To compare functional forms, note that for the two cases of isotropic scattering shown, $g_{1\langle\mathrm{DWS}\rangle}$ of Eq. (8) agrees better with g_{1Y} than $g_{1\mathrm{DWS}}$ of Eq. (7), whereas the opposite holds for the other two cases of anisotropic scattering. Furthermore, $g_{1\mathrm{DWS}}$ and $g_{1\langle\mathrm{DWS}\rangle}$ are both superior to $g_{1\mathrm{CT}}$ of Eq. (8) for isotropic scattering and no boundary reflections, the only case for which it is currently available.

Errors arising from the continuum approximations can be distinguished from errors arising from transport approximations using the same figure. Since $g_{1S} - g_{1Y}$ measures only the former, any deviation of $\Delta g_1(x)$ from $g_{1S} - g_{1Y}$ in Fig. 4 is entirely due to the latter. It is curious that $g_{1\mathrm{DWS}}$ agrees with g_{1S} better than both $g_{1\langle\mathrm{DWS}\rangle}$ and $g_{1\mathrm{CT}}$, since their transport approximations are not as severe. Furthermore, it is fortuitous that errors from the continuum and transport approximations are comparable in size and opposite in direction, at least for $L/l^* = 10$, giving analytic predictions closer to $g_{1Y}(x)$ than could have been expected.

The remaining plots show different measures of the transmission correlation function differences as a function of the optical thickness L/l^* of the slab, and should be useful for optimizing the accuracy of data analysis and estimating the remaining level of systematic error. The first, shown in Fig. 5 for four combinations of scattering anisotropy and boundary reflectivity, is an average absolute difference defined by

$$\langle |\Delta g_1| \rangle \equiv \int |g_1 - g_{1Y}| \, d \log_{10} x \ . \tag{13}$$

When $g_{1\langle\mathrm{DWS}\rangle}$ and $g_{1\mathrm{CT}}$ reach a minimum and then increase near the singularity at $x = 1$, and are hence unphysical, their values are set to zero in computing the above integral. Equation (13) is a useful average because the differences, as in Fig. 4 but irrespective of the value of L/l^*, are most significant over about one decade in x around $(L/l^*)^2 x \approx 10$, so that $\langle |\Delta g_1| \rangle$ is a robust indicator of the typical maximum difference. The results displayed in Fig. 5 all decrease rapidly with increasing L/l^*, and show that $g_{1\mathrm{DWS}}$ is the best functional form for very thin slabs and anisotropic scattering, while $g_{1\langle\mathrm{DWS}\rangle}$ is better for moderate to thick slabs and isotropic scattering. Whichever form is ultimately used for data analysis, systematic errors will be significant if experimental values of $g_1(\tau)$ are not all much greater than $\langle |\Delta g_1| \rangle$. Since experiments are usually performed on slabs of intermediate thickness, $7 < L/l^* < 20$, and $g_1(\tau)$ can easily be measured down to 0.03, systematic errors will be present according to Fig. 5 and care must therefore be taken.

Another measure of the accuracy of the predicted correlation functions is how well their small-x behavior agrees with that of $g_{1Y}(x)$ and can be judged in terms of a cumulant expansion $\ln[g_1(x)] = -\Gamma_1 x + \frac{1}{2}\Gamma_2 x^2 + \cdots$.
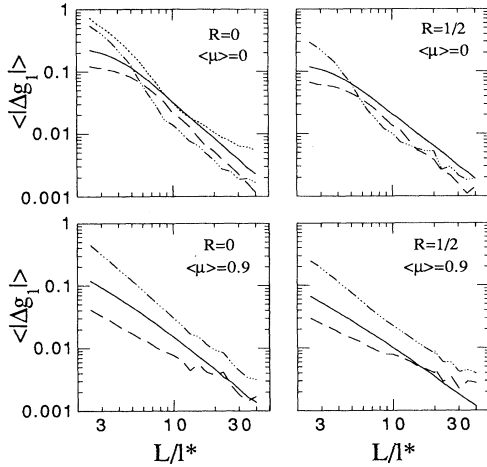
FIG. 5. Average absolute deviation between the approximate and benchmark correlation functions $\langle |\Delta g_1| \rangle$ defined by Eq. (13) vs optical thickness L/l^*. The solid curves are for $g_{1S}(x)$ of Eq. (6); the dashed curves are for $g_{1DWS}(x)$ of Eq. (7); the dash-dotted curves are for $g_{1\langle DWS \rangle}(x)$ of Eq. (8); and the dotted curve is for $g_{1CT}(x)$ of Eq. (9). Plots are labeled according to the boundary reflectivity R and the average cosine of the scattering angle $\langle \mu \rangle$.

The value of the first cumulant Γ_1 not only determines the small-x behavior, but also sets the scale for the full decay since $g_1(x)$ is nearly exponential in x. Figure 6 shows results for the decrease of the fractional deviation $\Delta \Gamma_1/\Gamma_1$ of the approximate cumulants from the benchmark cumulant of $g_{1Y}(x)$ as a function of increasing L/l^* for the same four combinations of scattering anisot-
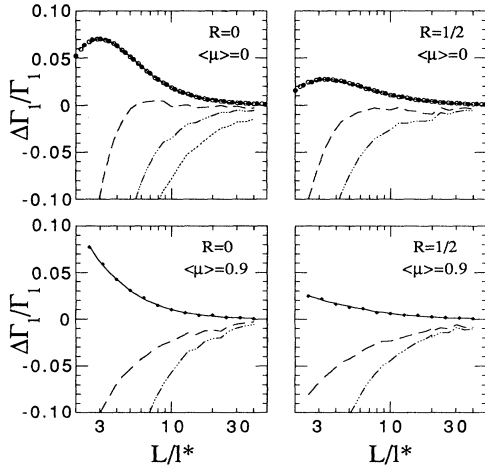

FIG. 6. Fractional difference in the approximate and benchmark correlation function cumulants vs optical thickness. The solid curves are for $g_{1S}(x)$ of Eq. (6); the dashed curves are for $g_{1DWS}(x)$ of Eq. (7); the dash-dotted curves are for $g_{1\langle DWS \rangle}(x)$ of Eq. (8); the dotted curve is for $g_{1CT}(x)$ of Eq. (9); and symbols are for previous $\langle S \rangle / \langle Y \rangle - 1$ data shown in Fig. 2. Plots are labeled according to the boundary reflectivity R and the average cosine of the scattering angle $\langle \mu \rangle$.

ropy and boundary reflectivity considered previously. Since $g_{1Y}(x) \approx 1 - x \langle Y \rangle /3$ and $g_{1S}(x) \approx 1 - x \langle S \rangle /3$ hold for small x, the fractional cumulant difference of $g_{1S}(x)$ from $g_{1Y}(x)$ is $\Delta \Gamma_1/\Gamma_1 = \langle S \rangle / \langle Y \rangle - 1$; the results from Fig. 2 for the fractional difference in the average dimensionless path length and total square wavevector transfer are therefore included in Fig. 6 as a check. In all cases shown, the cumulant of g_{1DWS} gives better agreement with the benchmark than that of either $g_{1\langle DWS \rangle}$ or g_{1CT}, but the degree of accuracy depends significantly on the scattering characteristics; the slab thickness must be greater than $L/l^* \cong 20$ for 1% accuracy if the scattering is highly anisotropic, but greater than only $L/l^* \cong 5$ if the scattering is isotropic. Such high accuracy in the first cumulant of g_{1DWS} is the fortuitous result of the partial cancellation of continuum and diffusive transport approximation errors.

If the functional form of the scatterer's dynamics $\langle \Delta r^2(\tau) \rangle$ is to be determined by inversion of $g_1(\tau)$ data, then the quantitative shape assumed for the correlation function is an important issue and is distinct from the overall rate of decay set by the first cumulant. For example, consider the case of perfectly diffusive dynamics $\langle \Delta r^2(\tau) \rangle = 6D\tau$. Inversion results for $\langle \Delta r^2(\tau) \rangle$ based on any of the theoretical forms of $g_1(x)$ in Eqs. (7)–(9) will show the correct behavior at short times $\langle \Delta r^2(\tau) \rangle \propto \tau$, and the constant of proportionality will simply be wrong by the cumulant difference shown in Fig. 5. At longer times, however, the inversion results for $\langle \Delta r^2(\tau) \rangle$ will not be proportional to τ because of inaccuracies in the theoretical shape assumed for $g_1(x)$. The following fractional difference corrects for the cumulant error and therefore serves to quantify the accuracy of the shape of $g_1(x)$:

$$\chi(x) = \frac{g_1(x\Gamma_{1Y}/\Gamma_1) - g_{1Y}(x)}{g_{1Y}(x)[1 - g_{1Y}(x)]} . \tag{14}$$

The difference is scaled in such a way as to emphasize that the accuracy of the theoretical form of $g_1(x)$ with respect to its distance from both 1 and zero are equally important; therefore, $\chi(x)$ also gives the level of systematic error present in inversion results for the functional form of the time dependence of $\langle \Delta r^2(\tau) \rangle$. Examples of the monotonic increase of $\chi(x)$ away from zero at small x are shown in Fig. 7 for fixed $L/l^* = 10$ and four combinations of boundary reflectivity and scattering anisotropy; without the cumulant correction in Eq. (14), $\chi(x)$ would begin at $\Delta \Gamma_1/\Gamma_1$.

Presuming that at least 1% accuracy is desired in the theoretical shape assumed for $g_1(x)$, it is useful to define $g_{1,min}$ as the value of $g_{1Y}(x)$ where $\chi(x) = 0.01$. If data analysis is then restricted to times τ small enough to satisfy $g_1(\tau) > g_{1,min}$, the functional form of inversion results for $\langle \Delta r^2(\tau) \rangle$ will be accurate to 1%; the overall proportionality factor will of course still be in error according to the cumulant difference plots of Fig. 6. Simulation results for $g_{1,min}$ so defined are shown vs L/l^* in Fig. 8 for the usual four cases of boundary reflectivity and scattering anisotropy; note that as L/l^* increases, the value of $g_{1,min}$ decreases, and therefore the range of
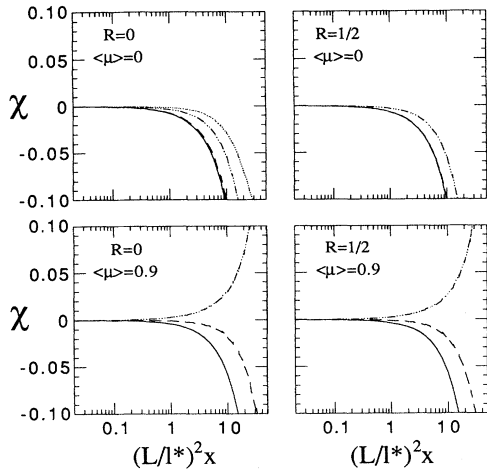
FIG. 7. Fractional error $\chi(x)$ defined by Eq. (14) in the shape of the approximate correlation functions in comparison with simulation results for the benchmark, as a function of the dimensionless dynamical variable $x = k^2 \langle \Delta r^2(\tau) \rangle$ for transmission through four slabs of optical thickness $L/l^* = 10$. The solid curves are for $g_{1S}(x)$ of Eq. (6); the dashed curves are for $g_{1\,\mathrm{DWS}}(x)$ of Eq. (7); the dash-dotted curves are for $g_{1\langle\mathrm{DWS}\rangle}(x)$ of Eq. (8); and the dotted curve is for $g_{1\,\mathrm{CT}}(x)$ of Eq. (9). Plots are labeled according to the boundary reflectivity R and the average cosine of the scattering angle $\langle \mu \rangle$.
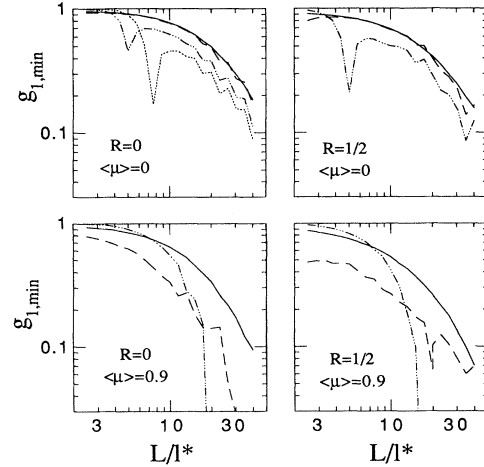

FIG. 8. Value of the correlation function above which the functional form of the predicted x dependence is accurate to 1%, i.e., $g_{1Y}(x)$ evaluated where $\chi(x) = 0.01$ vs optical thickness L/l^*. The solid curves are for $g_{1S}(x)$ of Eq. (6); the dashed curves are for $g_{1\,\mathrm{DWS}}(x)$ of Eq. (7); the dash-dotted curves are for $g_{1\langle\mathrm{DWS}\rangle}(x)$ of Eq. (8); and the dotted curve is for $g_{1\,\mathrm{CT}}(x)$ of Eq. (9). Plots are labeled according to the boundary reflectivity R and the average cosine of the scattering angle $\langle \mu \rangle$.

validity of the theories increases. Furthermore, since the values of $g_{1,\mathrm{min}}$ are not typically small in comparison with what can easily be measured, systematic errors in inversion results for the functional form of $\langle \Delta r^2(\tau) \rangle$ will be greater than 1% unless $g_1(\tau)$ data smaller than $g_{1,\mathrm{min}}$ are rejected. Caution should further be employed since $g_{1,\mathrm{min}}$ can have a dramatic L/l^* dependence. As for a comparison of theoretical forms for $g_1(x)$, note that while $g_{1\,\mathrm{DWS}}$ predicts the cumulant more accurately than $g_{1\langle\mathrm{DWS}\rangle}$, the shape of the correlation function is generally more accurately predicted by $g_{1\langle\mathrm{DWS}\rangle}$. For isotropic scattering with no boundary reflections, $g_{1\,\mathrm{CT}}$ has the best shape even though it is inferior by the previous comparisons.

The choice of 1% as the required accuracy for the predicted shape of $g_1(x)$ is, of course, arbitrary. If only 10% accuracy is desired, restrict attention to $g_1(\tau) > 0.2$ and $L/l^* > 10$.

III. CONCLUSIONS

The accuracy and range of validity of diffusing-wave spectroscopy theory predictions for the normalized electric field correlation function for photons transmitted through a slab have been determined by random walk computer simulations. For thin slabs, errors arise because of the presence of snakelike photon paths whose total square momentum transfer is significantly smaller than the continuum approximation proportionality to path length. Errors also arise for thin slabs because diffusive transport approximations cannot accurately ac-

count for the behavior of photons as they enter and leave the sample. The accuracy of the DWS theories is gauged by $\Delta\Gamma_1/\Gamma_1$, how well they predict the initial decay scale of the correlation functions; the simulation results of Fig. 6 indicate that in typical experimental situations the level of systematic error will be a few percent. The range of validity of the DWS theories is gauged by $g_{1,\mathrm{min}}$, the value of the benchmark correlation function below which the shape of the predicted correlation function deviates by more than 1%; the simulation results of Fig. 8 indicate than in typical experimental situations $g_{1,\mathrm{min}}$ is not small in comparison with what can be easily measured. Analysis of experimental $g_1(\tau)$ data should then be restricted to $g_1(\tau) > g_{1,\mathrm{min}}$ to avoid artifacts from fitting to an incorrect functional form; the fitting constants should then be accurate to a few percent according to the value of $\Delta\Gamma_1/\Gamma_1$. The trends found by simulation are that both $g_{1,\mathrm{min}}$ and $\Delta\Gamma_1/\Gamma_1$ decrease rapidly with increasing slab thickness, boundary reflectivity, and scattering anisotropy. Also, errors introduced by the continuum and diffusive transport approximations are found to partially cancel one another; therefore, both must be addressed simultaneously by any future analytic theory if it is to attain significantly greater accuracy. Alternatively, random walk simulation results for $g_{1Y}(x)$ can be used to analyze experimental data if higher precision is required.

[1] B. J. Berne and R. Pecora, *Dynamic Light Scattering: With Applications to Chemistry, Biology, and Physics* (Wiley, New York, 1976).

[2] B. Chu, *Laser Light Scattering: Basic Principles and Practice*, 2nd ed. (Academic, New York, 1991).

[3] K. S. Schmitz, *An Introduction to Dynamic Light Scattering by Macromolecules* (Academic, New York, 1990).

[4] *Dynamic Light Scattering: The Method and Some Applications*, edited by W. Brown (Clarendon, Oxford, 1993).

[5] G. Maret and P. E. Wolf, Z. Phys. B **65**, 409 (1987).

[6] M. J. Stephen, Phys. Rev. B **37**, 1 (1988).

[7] D. J. Pine, D. A. Weitz, P. M. Chaikin, and E. Herbolzheimer, Phys. Rev. Lett. **60**, 1134 (1988).

[8] J. X. Zhu, D. J. Durian, J. Müller, D. A. Weitz, and D. J. Pine, Phys. Rev. Lett. **68**, 2559 (1992).

[9] P. D. Kaplan, A. G. Yodh, and D. J. Pine, Phys. Rev. Lett. **68**, 393 (1992).

[10] A. Meller and J. Stavans, Phys. Rev. Lett. **68**, 3646 (1992).

[11] J. Z. Xue, E. Herbolzheimer, M. A. Rutgers, W. B. Russel, and P. M. Chaikin, Phys. Rev. Lett. **69**, 1715 (1992).

[12] S. Sanyal, A. K. Sood, S. Ramkumar, S. Ramaswamy, and N. Kumar, Phys. Rev. Lett. **72**, 2963 (1994).

[13] D. J. Durian, D. A. Weitz, and D. J. Pine, Science **252**, 686 (1991); Phys. Rev. A **44**, R7902 (1991).

[14] J. C. Earnshaw and A. H. Jaafar, Phys. Rev. E **49**, 5408 (1994).

[15] A. D. Gopal and D. J. Durian (unpublished).

[16] H. Gang, A. H. Krall, and D. A. Weitz, Phys. Rev. Lett. **73**, 3435 (1994).

[17] T. G. Mason and D. A. Weitz, Phys. Rev. Lett. **74**, 1250 (1995).

[18] D. J. Pine, D. A. Weitz, J. X. Zhu, and E. Herbolzheimer, J. Phys. (Paris) **51**, 2101 (1990).

[19] D. A. Weitz and D. J. Pine, in *Dynamic Light Scattering: The Method and Some Applications* (Ref. [4]), pp. 652–720.

[20] P. D. Kaplan, M. H. Kao, A. G. Yodh, and D. J. Pine, Appl. Opt. **32**, 3828 (1993).

[21] A. A. Middleton and D. S. Fisher, Phys. Rev. B **43**, 5934 (1991).

[22] D. J. Durian (unpublished).

[23] J. X. Zhu, D. J. Pine, and D. A. Weitz, Phys. Rev. A **44**, 3948 (1991).

[24] D. J. Durian, Phys. Rev. E **50**, 857 (1994).

[25] B. J. Ackerson, R. L. Dougherty, N. M. Reguigui, and U. Nobbmann, J. Thermophys. Heat Transfer **6**, 577 (1992).

[26] In addition to L. G. Henyey and J. L. Greenstein, Astrophys. J **93**, 70 (1941); see, for example, K. Kamiuto, J. Quant. Spectrosc. Radiat. Transfer **37**, 441 (1987); or G. C. Pomraning, *ibid.* **39**, 109 (1988).